Implantation and retrieval of magnetic nanobots for treatment of endodontic re-infection in human dentine

Dr. Debayan Dasgupta[1,5,#], Dr. Shanmukh Srinivas Peddi M.D.S.[1,5,#], Prof. Deepak Kumar Saini[2,3], and Prof. Ambarish Ghosh[1,4,5,*]

[1] Centre for Nano Science and Engineering, Indian Institute of Science, Bangalore 560012, India

[2] Department of Molecular Reproduction, Development and Genetics, Indian Institute of Science, Bangalore 560012, India

[3] Centre for Biosystems Science and Engineering, IISc, Bangalore 560012, India

[4] Department of Physics, Indian Institute of Science, Bangalore 560012, India

[5] Theranautilus Pvt. Ltd., Bangalore 560012, India

[#]Equal contributing authors
*Corresponding author

Keywords: *Nanobots*, *dentine*, *endodontic reinfection*, *active matter*, *root canal*

Abstract

More than 10% of root canal treatments undergo failure worldwide due to remnant bacteria deep in the dentinal tubules located within the dentine tissue of human teeth. Owing to the complex and narrow geometry of the tubules, current techniques relying on passive diffusion of anti-bacterial agents are inadequate. Here, we present a new treatment method using actively maneuvered nanobots, which can be incorporated during standard root canal procedure. Our technique will enable dentists to execute procedures inside the dentine not yet possible by current state of the art. We demonstrate that magnetically driven nanobots can reach the depths of the tubules up to hundred times faster than current clinical practices. Subtle modifications of the magnetic drive allowed deep implantation of the nanobots isotopically distributed throughout the dentine, along with spatially controlled retrieval from selected areas. Finally, we demonstrate the integration of bactericidal therapeutic modality with the nanobots, thereby validating the tremendous potential of nanobots in dentistry, and nanomedicine in general.

Introduction

Root canal treatment procedure is commonly prescribed to treat the infected pulp tissue of the human tooth[1]. Essential steps of the root canal treatment procedure involve careful removal of the pulp, followed by sterilization of the root canal space using harsh chemicals (sodium hypochlorite bleach[2], hydrogen peroxide,

EDTA[3] etc.) for mitigating the microbial load. 2.3 billion people suffer from dental caries worldwide[4] and almost 24-50 million(2004)[5] procedures are carried out in the US alone every year, of which more than 10% are reported to fail. A major cause of failure of root canal treatment is the persistence of bacteria within deep dentinal tubules, which are difficult to remove through conventional as well as state of the art techniques[2], [6]–[9], primarily due to the complex and narrow topography of the dentine tissue.

As shown in Figure 1(a), dentine tissue forms the bulk of a tooth structure which is covered with enamel and cementum on the crown and root respectively[10]. Dentine is characterised by the presence of hollow gradually tapering dentinal tubules traversing across its bulk from inner root canal space towards outer enamel or cementum (average tubule diameter changes from ~2.5 µm at the opening to ~0.9 µm near the cementum) (see Figure 1(b),1(c)). Lodged inside these intricate micro-tubular networks of dentinal tubules, the bacteria (common species: *Enterococcus faecalis*) are naturally protected from the host's defence system due to lack of local blood supply as shown by the schematic in Figure 1(d)[7], [11]. The effectiveness of current therapeutic entities to reach this depth of the dentinal tubules is limited by time, Δt of passive diffusion, with $\Delta t = L^2/D_m$, where L is the length inside the tubule and D_m is the diffusion constant of the drug molecules, although there have been efforts to augment the depth of delivery using ultrasound and optically induced forces[8], [9], [12].

Actively propelled micro/nano particles provide a novel way of targeting diseased sites at hard-to-reach places in the human body with cellular-level precision. Various techniques of manoeuvring nanobots (also referred to as nanomotors or nanopropellers in literature), using chemical[13]–[15], acoustic[16]–[19], magnetic[20]–[23], bio-hybrid[24]–[27] actuation methods, have been developed over the past decade. The time taken for external driven bots moving at constant speed u, varies as $\Delta t = L/u$, implying nanobots will be faster than passive diffusion beyond a certain depth. The idea is shown in Figure 1(e), where we compare nanobots moving at 0.8 μm/s (solid red) and 8 μm/s (dashed red) with passive diffusion of Alizarin dye molecules and 35 nm nanoparticles inside the tubules. Blue and green dots represent experimental data of the passive diffusion (see Materials and Methods section), with corresponding lines showing the time taken to vary as square of the covered distance. Clearly, the nanobots provide faster delivery for depths greater than few hundred microns, which forms the key motivation and clinical relevance of the experiments reported here.

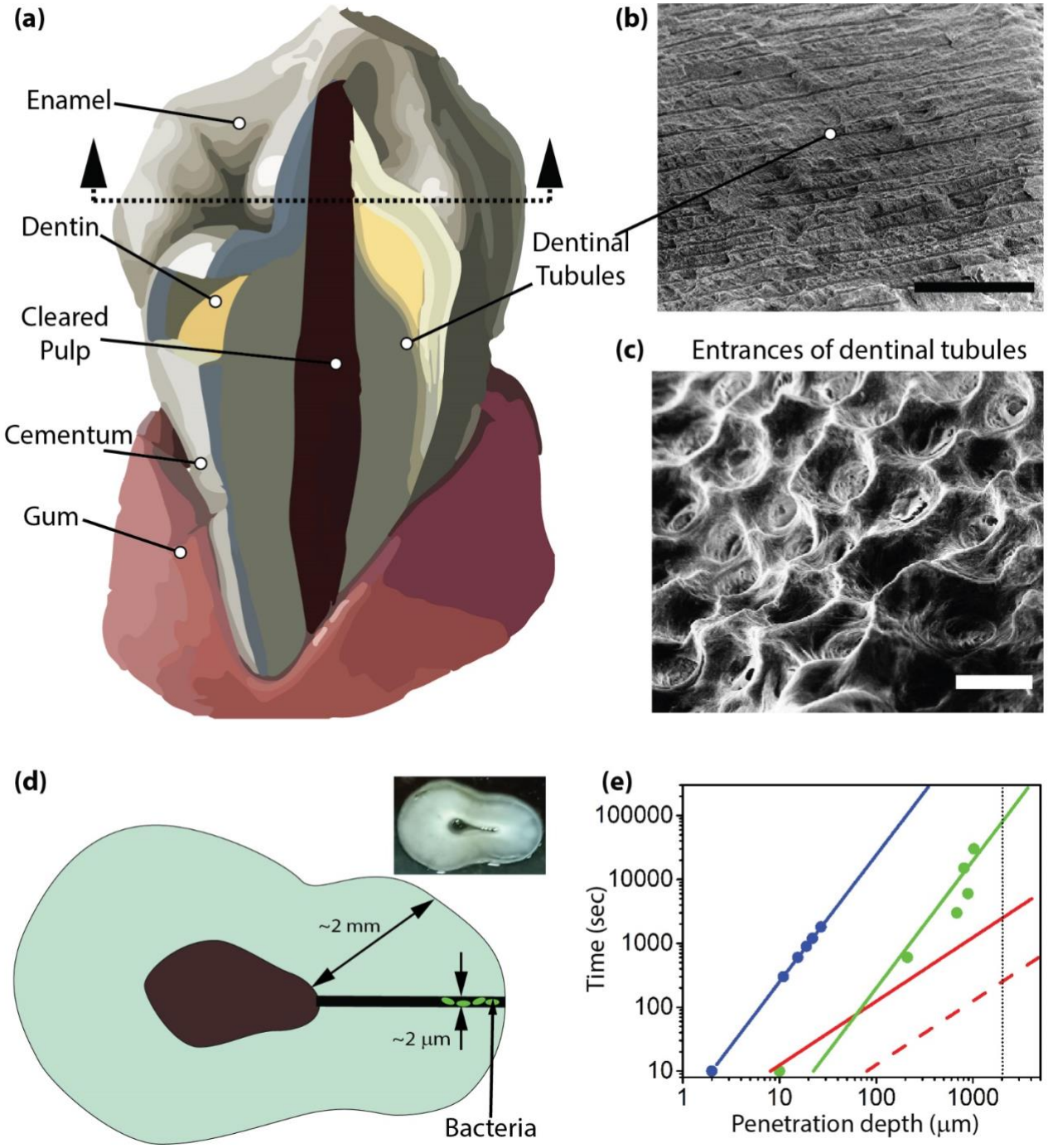

Figure 1:

(a) Schematic showing the anatomy of a typical human tooth. The pulp is cleared during the root canal treatment procedure, forming a cavity in the central canal, and exposing the dentine tissue. The dotted lines represent the cross-section plane. (b) Scanning electron microscope image of dentinal tubules. The channels formed by such tubules run deep into the dentine tissue. (scale bar 50 µm) (c) Close-up view of the entrance to the dentinal tubules as seen under a scanning electron microscope. (scalebar 5 µm) (d) Schematic representation of the cross-section of a human tooth. The central canal is shown in brown and a representation of a single dentinal tubule is shown in black. Persistent bacteria at the depths of the tubule are shown as green oval shapes. The cross-section of a representative sample used in our experiments is shown in the inset. (e) Comparison of time taken to achieve a penetration depth for 35 nm nanoparticles (shown in blue, dots represent experimental data, and a linear fit is shown by the solid line), alizarin dye (shown in green, dots represent experimental data, and a linear fit is shown by the solid line), nanobots swimming with a velocity of 0.8 µm/sec (shown in solid red line) and nanobots swimming with a velocity of 8 µm/sec (shown in dashed red line). Clinically relevant maximum depth of 2000 µm is shown as the vertical black dotted line.

Results:

The experimental platform of the magnetic nanobots used in the present studies was based on helical nanostructures driven by rotating magnetic fields through intrinsic rotation-translation coupling of the chiral structure. The experimental system has been described in detail before[28], [29] and in the supplementary information (see Section S1), and shown to be highly promising for various sensing[30]–[33], therapeutic[34]–[36] and cargo towing applications[37], [38] in microfluidic, as well as *ex vivo* and *in vivo* biological environments. We use a fabrication method based on shadow evaporation to form helical nanostructures (yielding few billion nanobots per evaporation) that allows us to impart multiple functionalities, such as chemical[35], [36], [39], magnetic[24], [40], plasmonic[37], [38], hyperthermia[34] capabilities within a single nanohelix. The manipulation is carried out using small (< hundred gauss) rotating magnetic fields that drives the helices along the direction specific by the sense of rotation of the field and the handedness of the helix.

The experimental protocol is shown in the schematic of Figure 2(a), where nanobots were driven inside the tubules, powered by a rotating magnetic field, propelled into the depths of the tubules where bacteria usually reside. In all our experiments, nanobots suspended in de-ionized water was injected in the cleared central canal of an *ex vivo* tooth sample. The nanobots were actuated for 20 minutes using 50 Gauss magnetic field rotating at 5 Hz and were subsequently imaged by electron microscopy. SEM images confirmed the successful penetration of the nanobots about 1000 μm deep into the tubules, as shown in Figure 2(b). The nanobots were aligned to the tracks of the tubule, indicating they were not disturbed during the physical process of splitting the teeth longitudinally for sample preparation.

After demonstrating the feasibility of reaching great depths in the dentinal tubules using scanning electron microscopy; for quantitative studies, we used fluorescence microscopy to visualize the nanobots inside the tubules. This was performed with various fluorophores, including upconversion (NIR) nanoparticles (see Materials and Methods). Most of the experiments presented in this paper was carried out by labelling the bots with 6-aminofluroscein (see Materials and Methods for detailed protocol). In the demonstration shown in Figure 2(c), the nanobots were driven back and forth by periodically reversing (about every 180 seconds) the sense of rotation of the field (strength 30 gauss and frequency 5 Hz). Close inspection of the trajectory reveals the bots to follow the physical space defined by the tubules in a direction determined by the field (see Movie M1). As far as we know, this is the first live demonstration of an externally maneuvered nanostructure within the dentinal tubules.

The schematic shown in Figure 2(d) shows the approach of positioning nanobots inside the dentine. Fluorescently labelled nanobots suspended in de-ionized water were driven from the central canal into the dentinal tubules using a magnetic drive. The cross-section of the human tooth used for our experiments was about 200 μm in thickness, of which about a 10 μm thick slice was observed by a confocal microscope. The average direction in which the nanobots moved due to the magnetic drive could be seen from stacking about

100 confocal slices and observing the fluorescent nanobots. We included both right- and left-handed helices within the suspension to achieve higher coverage, which would move along opposite directions due to the Baranova effect [41], arising due to the opposite sign of the rotation-translation coupling term in the mobility tensor of right versus left handed helices. Demonstration with many nanobots under the drive of rotating fields of strength 50 Gauss and frequency of 5 Hz, carried over 20 minutes, is shown in Figure 2(e). As seen in the maximum intensity projection of confocal stacks in Figure 2(e) the spatial depth distribution of nanobots were roughly diametrically opposite to each other.

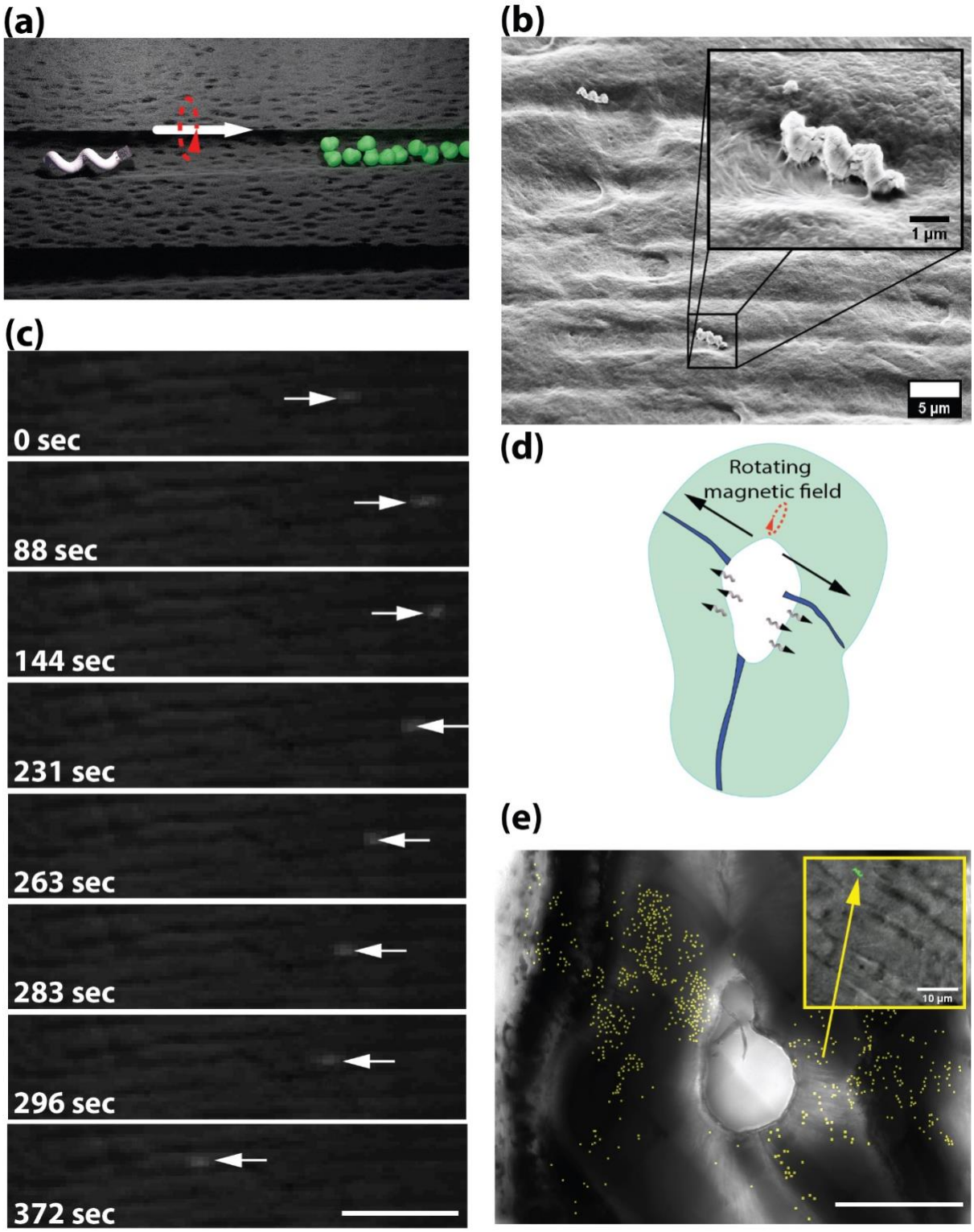

Figure 2:

(a) Schematic showing a nanobot driven by rotating magnetic fields deep into a dentinal tubule, such as to reach the location of persistent bacteria (shown in green). (b) A longitudinal view of the dentine tissue where the nanobot was driven ~1000 µm inside the depth of the tubules as measured from the entrance at the central canal. (c) Various snapshots from a movie where the bot was maneuvered forward and backward through a dentinal tubule. The scale bar represents 10 µm. (d) Schematic showing direction of motion of nanobots with opposite chirality under the influence of rotating field. (e) Maximum intensity projection of 150 confocal slices showing nanobots of opposite chirality subjected to a rotating magnetic field. For clarity we have highlighted the locations of the nanobots with a yellow overlay. The scale bar represents 500 µm.

While directed motion using a rotating magnetic field is a promising strategy for targeting specific regions, this approach is not optimal to achieve uniform spread of nanobots throughout the dentine. One possibility is to sequentially change the direction of rotating field to achieve a sector-by-sector targeting; however, this strategy is time consuming and prone to depletion of nanobots from the suspension. Described next is a significantly more efficient strategy, using oscillating magnetic fields to induce a rocking motion in all the helical nanobots present within the sample, which results in their net motion along the length of the tubules, irrespective of which way the tubules are oriented (see schematic in Figure 3(a)).

The microscopic mechanism in which motility is induced in the nanobots without specifying their direction is relevant to rendering the helices self-propelled and been discussed in the past[40], [42]–[44]. In summary, oscillating fields result in reciprocal (back and forth) motion of the nanohelices, which results in enhanced diffusivity. In the presence of a surface and certain geometrical asymmetries, the helices may also achieve net motion, for example as shown in schematic of Figure 3(b) (see Movie M2). The concentration of magnetic metals at the tip of the helix can introduce an asymmetry in the weight, making one end of the nanobot pivot towards the surface. The tip of the helix closer to the surface would experience increased drag while being rotated and therefore translated slightly towards the surface. However, during the half-turn that propels the nanobot away from the surface, it experiences lower drag and thus can move farther. This asymmetry in translational motion during a back-and-forth cycle, when repeated over a long time can result in a net displacement of the particle along a certain direction.

While in the central canal, a nanobot executing such reciprocal motion would spread isotropically due to diffusion, with a possible small enhancement in diffusivity. When it reaches the entrance of a tubule, there is a finite probability for the bot to get in. Once inside the tubule, the geometry of the tube guides the nanobot through a quasi-one-dimensional path. Nanobots interacting with the surface of the dentinal tubule can follow the tubule trajectory and reach the depths where bacterial colony resides. A uniform distribution of nanobots from the central canal can be seen in the tooth cross section of Figure 3(c) which show a maximum intensity projection of 100 confocal stacks representing a thickness of 100μm. The fluorophore coated nanobots are highlighted in yellow, to show the uniformity in angular distribution.

In addition to the high coverage achievable through the oscillating magnetic drive, a particularly attractive possibility is related to bot-mediated sterilization of the apical third section of the teeth. This is a daunting task for endodontists because a tooth's root anatomy towards its apical portion becomes progressively more complicated[45] as the corresponding central root canal's orifice becomes progressively smaller, with increased chances of canal ramifications, unpredictable canal curvatures and dwindling number of dentinal tubules. Indeed, such hard to reach places provide a challenge which externally maneuvered bots are well-suited to solve. We have maneuvered nanobots into dentinal tubules of a tooth section prepared selecting 3 mm distance from root apex, such as to test their presence at apical portions of the root with similar results (see Figure 3(d)).

In Figure 3(e), we show a comparison of the distribution achieved by different driving mechanisms. Nanobots with opposite chirality subjected to a rotating magnetic field show a bimodal angular distribution, where the opposite sectors of the dentine are targeted. The maximum number of nanobots were found at 40° and 190° as measured from the axis coinciding with the major and minor axis of the elliptical shape. While we expected the angular distribution to show peaks that are 180°apart, the experimental difference of 150° was due to the dentinal tubules bending away from their entrance angles, as they grew deeper into the dentine, and has been well documented in the dental literature. For the nanobots subjected to an oscillating magnetic field with amplitude 60 Gauss and oscillating frequency of 40 Hz for 20 minutes, the maximum depth achieved by the nanobots were about ~1200 μm inside the dentine, with uniform angular distribution. The average pitch with rotating drive was 18 nm ± 6 nm (mean ± standard deviation) which was higher by 50% compared to oscillating drive where the average pitch was 9 ± 3 nm (mean ± standard deviation). Taken together, we envision rotating drives for known and direct spatial targeting applications, while oscillating drives useful for maximal coverage of the dentine.

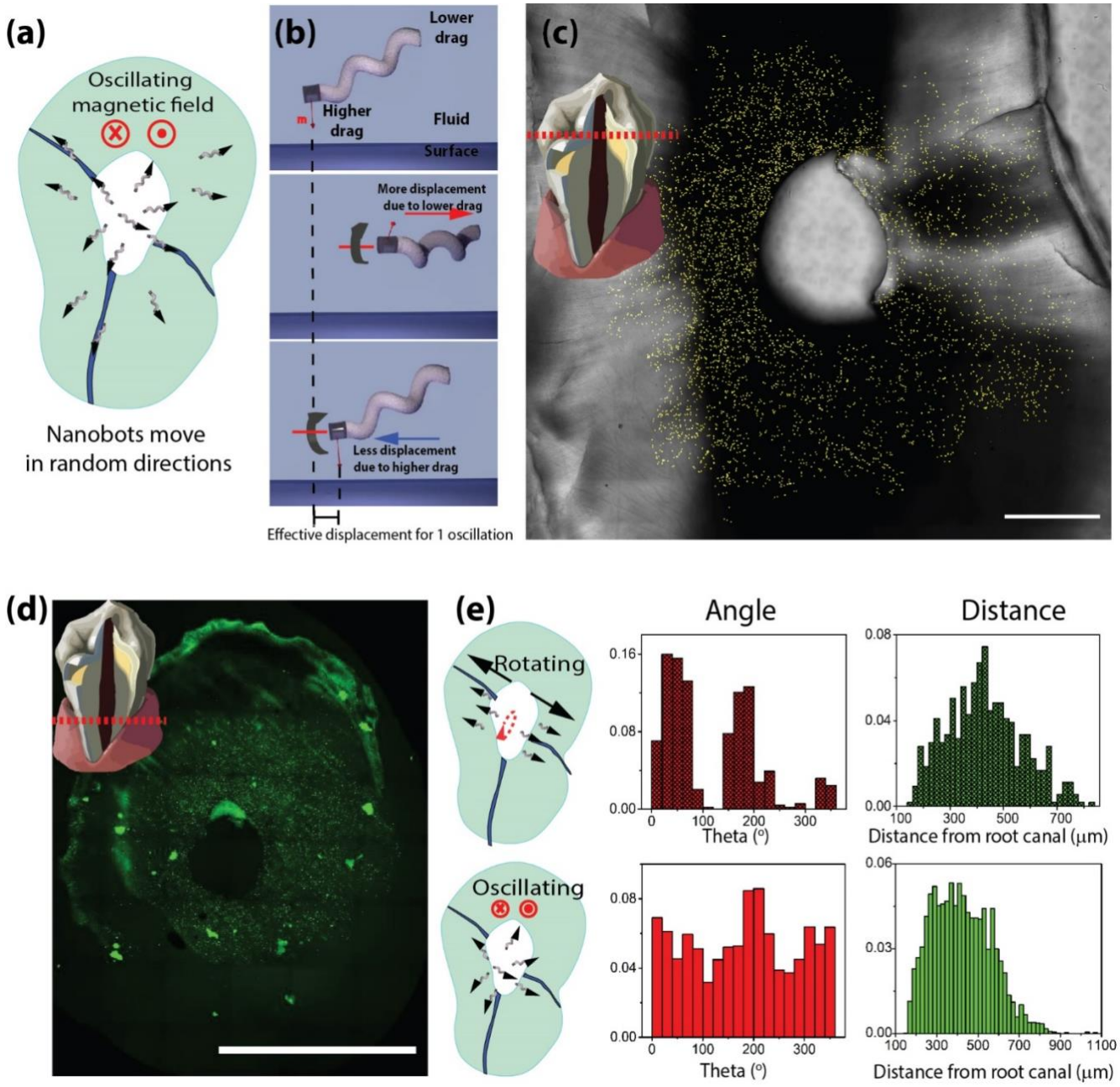

Figure 3:

(a) Schematic showing distribution of nanobots under oscillating field. The direction of oscillation in perpendicular to the plane of the cross-section, as shown by the red cross and dot markers. (b) Schematic showing the mechanism of motion of nanobots under the influence of oscillating field near a surface. (c) Maximum intensity projection of 100 confocal slices showing distribution of nanobots under oscillating field. The scale bar represents 500 µm. (d) Maximum intensity projection of 100 confocal slices showing the distribution of nanobots in the apical portion section. Scale bar represents 100 µm. (e) Comparison of angular distribution, distance distribution, and average velocity for rotating and oscillating magnetic field

While the previous demonstrations show the nanobots to be suited for targeted as well as isotropically distributed nanoscale implants, in the following section, we show how the bots can be retrieved from specific regions of tubules. As shown in the schematic Figure 4(a), the bots were driven into the tubules using an oscillating field as a first step. For this experiment, the magnetic field of strength 50 G was oscillated at 40 Hz for 8 minutes. This ensured a uniform distribution of nanobots into the tubules. After

subjecting the nanobots to an oscillating field, the field configuration was switched to a rotating field along one direction to drive out nanobots from one section of the dentine tissue for the second step of the experiment, as shown in the schematic Figure 4(a). The field strength was kept at 50 G, rotating at 40 Hz for 10 minutes. As shown in Figure 4(b), the lower right corner of the cross-section has very few nanobots than the rest of the dentine, proving it is indeed possible to retrieve nanobots from dentine once their therapeutic activity has been achieved, and when the presence of nanobots in the dentine is not necessary anymore.

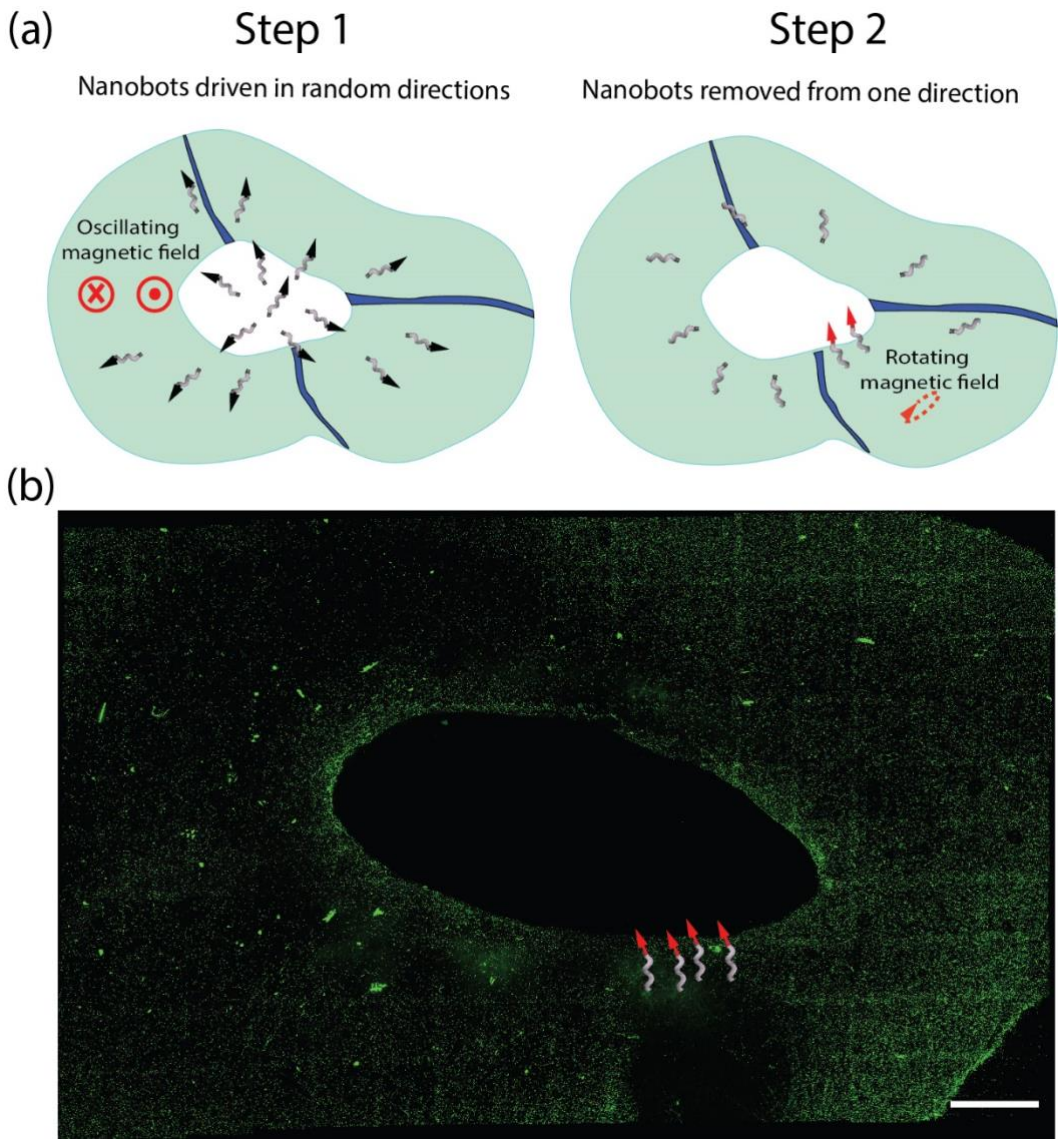

Figure 4

(a) Schematic showing the experimental procedure followed to demonstrate retrieval of nanobots. In Step 1, nanobots were subjected to oscillating magnetic field to drive them randomly inside dentinal tubules. In Step 2, a rotating magnetic field was applied along a single direction to empty a sector of the tooth. (b) Maximum intensity projection of 150 confocal slices showing distribution of fluorescent nanobots. The empty space at the lower right corner shows the space from which nanobots were retrieved. The scale bar represents 500 µm.

There have been multiple therapeutic modalities, such as liposomes[26], [27], delivery of nuclear materials such as siRNA[46], magnetic hyperthermia[34], [47] etc integrated with nanobots, including anti-microbial properties. We believe many of these functionalities can be incorporated with the present system of helical, magnetic nanobots as well for efficient sterilization of the dentine during the root canal procedure. As a proof of concept, we have integrated hyperthermia-based therapeutic potential as possible anti-microbial strategy, by using the magnetic layer (here, iron) of the nanobots as localized heat sources under rapidly varying magnetic fields. As shown in the inset in Figure 5(a), a teeth cross section was placed inside the magnetic hyperthermia coil. One side of the teeth was treated with high dosage of nanobots ($>10^9$ nanobots) whereas the other side was relatively scarcely populated with nanobots. After 15 minutes of exposure to a 40 kA/m oscillating magnetic field at a frequency of 240 kHz, a temperature difference was observed on the side of the tooth containing more bots. This temperature difference was captured by an IR thermal camera as shown in Figure 5(a). While the overall gain in temperature, when measured by an IR camera appears to show only a 1°C rise due to the presence of nanobots inside the tubules, the local temperature rise in the vicinity of nanobots is expected to be much higher. We further confirmed that the heat generated at the surface of the bots was sufficient to eradicate *E.faecalis*, which is known to be the primary cause of endodontic reinfection and one of the most resistant bacteria found in the human microbiome. We placed nanobots on agar cultures of green fluorescent protein (GFP) expressing *E.faecalis*. After the hyperthermia treatment, the agar plate was treated with propidium iodide (PI) which served as an indicator for dead cell population. The results as shown in Figure 5(b) indicates that bacteria death can be colocalized to the nanobots which act as heat source.

Utilizing localized heat as therapeutic treatment of bacteria within dentinal tubules is demonstrated in Figure 5(c). *E. faecalis* bacteria was allowed to enter the dentinal tubules by dipping and centrifuging the tooth cross-section repeatedly in a bacterial culture suspended in BHI broth with the entrance to the dentinal tubules exposed to the culture media (see Materials and Methods for bacterial culture details). Nanobots were driven using oscillating fields, following which the cross-section was split from the middle. One split section was subjected to magnetic hyperthermia for 10 minutes whereas the other section was preserved as a control. From visual inspection, it became clear that more *E.faecalis* stained red with PI were present in the section that was subjected to hyperthermia, indicating higher bacterial death. This was further confirmed in Figure 5(d) where the same tooth section was used as a control. For the experiment shown in Figure 5(d), the cross-section was filled with *E. faecalis* by repeatedly dipping the tooth in bacterial suspension. This allowed bacteria to enter dentinal tubules along all directions. Nanobots were driven along a single direction using a rotating magnetic field of 50 G rotating at 20 Hz for 10 minutes. The direction was so chosen to align with the short axis of the elliptically shaped cross-section of the tooth. After driving the nanobots inside the tubules, the sample was subjected to magnetic hyperthermia for 15 minutes. The tooth section was then treated with PI stain to mark for bacterial death. A red band of dead bacteria can be clearly seen in the middle of the tooth section in Figure 5(d).

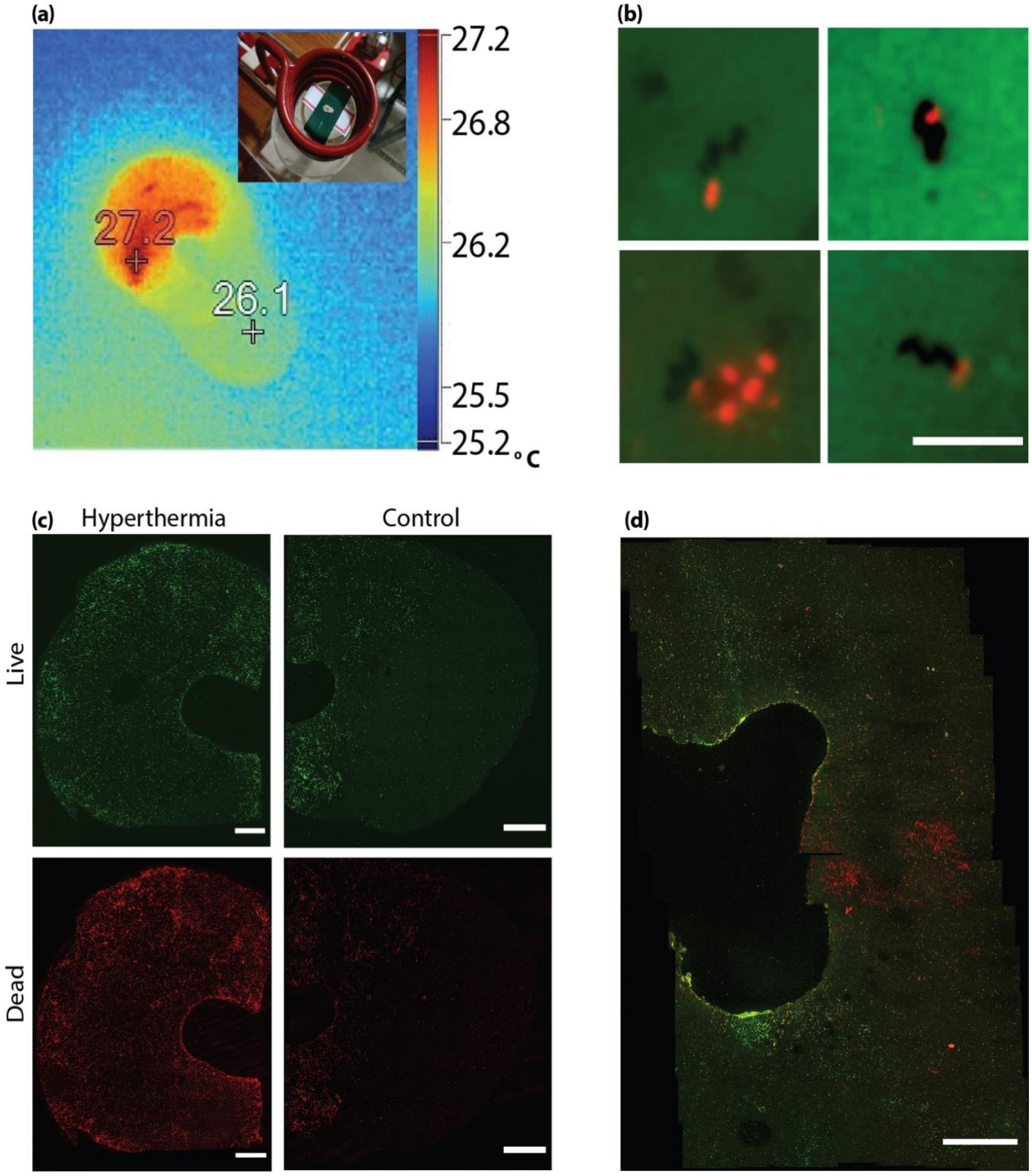

Figure 5:

(a) Infrared image of the tooth sample taken after subjecting it to magnetic hyperthermia for 15 minutes. The presence of iron-rich nanobots driven on one side of the tooth produces a distinct temperature gradient due to magnetic heating. Experimental setup showing a human tooth cross-section inside a magnetic hyperthermia coil in shown in the inset. (b) Series of images where dead bacteria (stained in red) are collocated near nanobots, which act as localized heat source. Green indicates live bacteria which is expressing green fluorescent protein. Scale bars represent 5 µm. (c) Maximum intensity projection of ~20 confocal stacks showing bacterial death inside dentinal tubules. The number of dead bacteria (stained red due to PI) is higher in the tooth segment subjected to hyperthermia. Scale bar represents 100 µm. (d) Maximum intensity projection showing selectivity in bacterial death inside dentinal tubules. Bacteria was allowed to move inside tubules along all directions. Nanobots were driven along a single direction using rotating field, following which the sample was subjected to magnetic hyperthermia. Bacterial death is observed along a band in the centre where more bacteria were stained red. Scale bar represents 100 µm.

Discussion:

We present a new efficient method of sterilizing the dentine tissue of human teeth during the root canal procedure to prevent endodontic reinfection. We have demonstrated how magnetically actuated helical nanobots can be used to improve access to the depth of the dentinal tubules where persistence of bacteria is the main cause of endodontic reinfection. We demonstrate that nanobots can be used to target specific sectors of the dentine using rotating magnetic fields and achieve isotropic coverage under oscillating drive. We have further demonstrated how a combination of rotating and oscillating fields may be used to remove nanobots from the dentine, which could be useful for applications where it is desirable to retrieve nanobots after the therapy is delivered.

It is interesting how the system of helical magnetic nanobots can be used for direct spatial targeting, as well as applications requiring fast and uniform coverage. In the latter, motility is induced externally, where the directionality arises through the natural tracks provided by the topography of the dentine. These capabilities exist in few artificial nanobot systems[14], [17], [48], [49], and provide a natural advantage compared to passively diffusing drug-loaded nanoparticles using in conventional nanomedicine. As a further step to the utilization of this technology in treating endodontic reinfection, we have proposed a heat based bactericidal method, where the magnetic layer embedded in the nanobots can be converted to a localised heat source. Finally, one must recognize that the bots used in our experiments were made of silica and iron, which have been shown to be biocompatible by numerous previous experiments[31], [36], [50]–[53]. From a clinical perspective, while a single dose of treatment with nanobots may reduce the bacterial load substantially following which they may be retrieved, owing to the resilient nature of *E.faecalis*, an option for reheating and thereby sterilizing the tubules in future may also be a practical option.

Acknowledgement:

We acknowledge the Nanobio team, and Reshma V.R. for helpful discussions and for her support with experiments. We are grateful for the technical support from the IISc Bioimaging facility. This research was supported in part by DBT and DST-SERB. DDG would like to thank IISc and the Ministry of Human Resource Development (MHRD), Government of India for providing the Senior Research Fellowship (SRF). We also acknowledge funding from MHRD, MeitY and DST Nano Mission for supporting the facilities at CeNSE. DS and AG acknowledges funding from the IISc Biosciences division for supporting this collaborative project.

Conflict of Interest:
D.D., S.S. and A.G. declare financial interests in Theranautilus. This biotechnology company is developing similar technology for medical applications. The remaining author declares no competing financial interests.

Movie List:

1. Video showing motion of nanobot in tubules
2. Schematic representation of motion due to oscillating field in the presence of surface

Materials and methods:

Tooth sample preparation:

Freshly extracted, intact, single canalled mandibular teeth specimens (from age group ranging from 25-45 years) free of any cervical and carious lesions were stored in Phosphate Buffered Saline (PBS). The presence of a single canal was reconfirmed through radiographic assessment; every specimen was sectioned at a 14mm length from their morphological root apex using a low-speed IsoMet–1000 saw (Buehler, USA). The working length was set at 13mm (1mm short of the root apex). To achieve a standard root canal preparation all the specimens were instrumented using ProTaper Gold rotary files (DENTSPLY Maillefer, Ballaigues, Switzerland) up to file sequence F3 (master apical file). During and after instrumentation the root canals were irrigated (rinsed) with 17% Ethylenediaminetetraacetic acid (EDTA; Sigma Aldrich, USA) followed by treatment with 5.25% Sodium hypochlorite using 30 gauge syringe needle to remove the smear layer. After the instrumentation procedure, final rinse of the root canal was performed using PBS. Following instrumentation procedure, the teeth specimens were cross-sectioned at a uniform thickness of 400µ using a low-speed IsoMet-1000 saw (Buehler, USA).

Nanobot Fabrication:

The helical nanobots were fabricated using Glancing Angle Deposition (GLAD) technique and the seeding layer type employed was Lightsmyth pattern (LIL) with silica pillars of diameter ~ 250nm, height ~ 1µ and an average spacing (amongst adjacent silica pillars) of ~700nm. Silica helices were grown onto the seeding layer using GLAD where a material flux comes at an extreme angle (~ 5 degrees) while the seeding layer is rotated at a certain rate depending on the selected geometry of helices. The characteristic diameter of each silica pillar in the seeding layer determines a fabricated nanobot's thickness, while length and pitch of a nanobot are determined by the time and the rotation rate of a seeding layer (mounted on the GLAD platform) respectively. The spatially specific composition of a nanobot is controlled by a predetermined sequencing in the deposition of the material of choice; initially, 5nm of silver, 50nm of silica, 10nm of pure iron, and 50nm of silica were deposited sequentially (and respectively) without rotating the seeding layer to form a pure iron-cored silica blob-head. Subsequently, this initial step was followed by a concomitant controlled rotation of GLAD platform (1˚ rotation for every 3.4nm substrate deposition) and deposition with silica as the material of choice; this step is continued till a total deposition thickness (vertical) of 3µm is achieved.

Nanobot - Fluorophore Conjugation:

Seed layer with standing nanobots was first plasma cleaned at 0.517 bar atmospheric pressure for 15 minutes to remove surface impurities. After the plasma cleaning process, the seed layer was transferred into an Eppendorf tube containing 65.8µL of [3-(Trimethoxysilyl) propyl] succinicanhydride (TEPSA) (TCI Chemicals, India) in 934.2µL of N, N-Dimethylformamide (DMF) (Sigma Aldrich, India) solution along with 100µL of deionized water and 100µL of Tetrabutylammonium hydroxide (Sigma Aldrich, India); mentioned

Eppendorf tube setup is kept overnight in a water bath at a temperature of 120°C. Following day the seeding layer is transferred into a new Eppendorf tube and washed three times consecutively with DMF solution and Deionized water. Post-washing the seeding layer is transferred into an amber-tinted Eppendorf tube containing a solution of 10mg of 1-Ethyl-3-[3-dimethylaminopropyl]-carbodiimide hydrochloride (EDC) (Sigma Aldrich, India), 10mg of N-hydroxysuccinimide (NHS) (Sigma Aldrich, India), 10mg of 6-aminofluroscein (Sigma Aldrich, India) in 500 µL of 2-(N-morpholino)ethanesulfonic acid (MES) (Sigma Aldrich, India) buffer (0.1M, 4.7pH), and 500 µL of Dimethyl Sulfoxide (Sigma Aldrich, India). The whole setup is kept overnight on a rocker, followed by gently washing the seeding layer with phosphate-buffered saline. The fluorescent nanobots were excited at 490nm and they have strong emission at 520 nm.

***Enterococcus Faecalis* Culture**:

E. Faecalis standard strain (American Type Culture Collection 29212) expressing green–fluorescent protein (GFP) was obtained through electroporation with pMV158-GFP plasmid [10] and was kind gift from Prof. V. Singh, IISc. Transformed recombinant bacteria were selected through the addition of following antibiotics: chloramphenicol 4µg/ml, tetracycline 4µg/ml and erythromycin 30 µg/ml. Recombinant GFP expressing *E.Faecalis* were inoculated into 10ml brain-heart infusion (BHI) culture broth (34g/ 1L; Merck, Darmstadt, Germany), antibiotics tetracycline 4µg/ml, and erythromycin 2.5µg/ml (10mg/ml) were added to the broth to maintain recombinant *E. faecalis* bacterial culture, at 37°C for 12 hours.

Nanobot - Upconversion Conjugation:

Seed layer with standing nanobots is first plasma cleaned at 0.517bar atmospheric pressure for 15 minutes to remove surface impurities. After the plasma cleaning process, the seed layer is transferred into an Eppendorf tube containing 940µl of ethanol, 40µl of deionised water and 20µl of (3-Aminopropyl) triethoxysilane (APTES; Sigma Aldrich, India). The Eppendorf tube setup is subjected to water-bath for 12 hours maintained at a temperature of 60° C. After 12 hours of water-bath treatment the seed layer is salvaged from the Eppendorf tube and laid on a flat surface with standing nanobots facing upwards (exposed surface); in a separate Eppendorf tube 5mg of EDC (Sigma Aldrich, India) and 5mg of NHS (Sigma Aldrich, India) are added onto 30 µl solution of MES buffer (Sigma Aldrich, India; 0.1M, 4.7pH). This solution is transferred onto the exposed surface of the seeding layer followed by drop-casting of 10 µl of Upconversion nanoparticles (particle size 35nm; Sigma Aldrich, India). The drop-casted seed layer is left to dry consequently rinsing it gently for 3 times with deionised water.

References:

[1] K. M. Hargreaves, L. H. Berman, and I. Rotstein, *Cohen's Pathways of The Pulp 11th Ed.* 2016.

[2] M. Guivarc'h, U. Ordioni, H. M. A. Ahmed, S. Cohen, J. H. Catherine, and F. Bukiet, "Sodium Hypochlorite Accident: A Systematic Review," *Journal of Endodontics*. 2017, doi: 10.1016/j.joen.2016.09.023.

[3] C. Solana, C. M. Ferrer-Luque, X. Wang, P. Baca, M. Ruiz-Linares, and T. Cabrera, "Cytotoxic effects of alkaline tetrasodium edta irrigating solutions," *J. Oral Sci.*, 2020, doi: 10.2334/josnusd.19-0234.

[4] E. Bernabe *et al.*, "Global, Regional, and National Levels and Trends in Burden of Oral Conditions from 1990 to 2017: A Systematic Analysis for the Global Burden of Disease 2017 Study," *Journal of Dental Research*. 2020, doi: 10.1177/0022034520908533.

[5] R. Wong, "Conventional endodontic failure and retreatment," *Dental Clinics of North America*. 2004, doi: 10.1016/j.cden.2003.10.002.

[6] K. M. Galler *et al.*, "Penetration depth of irrigants into root dentine after sonic, ultrasonic and photoacoustic activation," *Int. Endod. J.*, 2019, doi: 10.1111/iej.13108.

[7] A. R. Vieira, J. F. Siqueira, D. Ricucci, and W. S. P. Lopes, "Dentinal tubule infection as the cause of recurrent disease and late endodontic treatment failure: A case report," *J. Endod.*, 2012, doi: 10.1016/j.joen.2011.10.019.

[8] D. Li, S. Jiang, X. Yin, J. W. W. Chang, J. Ke, and C. Zhang, "Efficacy of needle, ultrasonic, and endoactivator irrigation and photon-induced photoacoustic streaming in removing calcium hydroxide from the main canal and isthmus: An in vitro micro-computed tomography and scanning electron microscopy study," *Photomed. Laser Surg.*, 2015, doi: 10.1089/pho.2015.3903.

[9] H. H. Peeters and N. Gutknecht, "Efficacy of laser-driven irrigation versus ultrasonic in removing an airlock from the apical third of a narrow root canal," *Aust. Endod. J.*, 2014, doi: 10.1111/aej.12016.

[10] A. Nanci, "Ten Cate's Oral Histology - E-Book: Develpment, Structure and Function," *Struct. Oral Tissues*, 2018.

[11] C. H. Stuart, S. A. Schwartz, T. J. Beeson, and C. B. Owatz, "Enterococcus faecalis: Its role in root canal treatment failure and current concepts in retreatment," *Journal of Endodontics*. 2006, doi: 10.1016/j.joen.2005.10.049.

[12] Nct, "Effect of Passive Ultrasonic Irrigation on Success of Primary Endodontic Treatment," *https://clinicaltrials.gov/show/NCT02632513*, 2015.

[13] K. K. Dey and A. Sen, “Chemically Propelled Molecules and Machines,” *J. Am. Chem. Soc.*, vol. 139, no. 23, pp. 7666–7676, Jun. 2017, doi: 10.1021/jacs.7b02347.

[14] W. F. Paxton *et al.*, “Catalytic nanomotors: Autonomous movement of striped nanorods,” *J. Am. Chem. Soc.*, 2004, doi: 10.1021/ja047697z.

[15] K. K. Dey *et al.*, “Micromotors Powered by Enzyme Catalysis,” *Nano Lett.*, vol. 15, no. 12, pp. 8311–8315, Dec. 2015, doi: 10.1021/acs.nanolett.5b03935.

[16] J. M. McNeill, N. Nama, J. M. Braxton, and T. E. Mallouk, “Wafer-Scale Fabrication of Micro- to Nanoscale Bubble Swimmers and Their Fast Autonomous Propulsion by Ultrasound,” *ACS Nano*, 2020, doi: 10.1021/acsnano.0c03311.

[17] W. Wang, S. Li, L. Mair, S. Ahmed, T. J. Huang, and T. E. Mallouk, “Acoustic Propulsion of Nanorod Motors Inside Living Cells,” *Angew. Chemie Int. Ed.*, vol. 53, no. 12, pp. 3201–3204, Mar. 2014, doi: 10.1002/anie.201309629.

[18] W. Wang, L. A. Castro, M. Hoyos, and T. E. Mallouk, “Autonomous motion of metallic microrods propelled by ultrasound,” *ACS Nano*, vol. 6, no. 7, pp. 6122–6132, Jul. 2012, doi: 10.1021/nn301312z.

[19] A. L. Balk *et al.*, “Kilohertz rotation of nanorods propelled by ultrasound, traced by microvortex advection of nanoparticles,” *ACS Nano*, 2014, doi: 10.1021/nn502753x.

[20] A. Ghosh and P. Fischer, “Controlled propulsion of artificial magnetic nanostructured propellers,” *Nano Lett.*, vol. 9, no. 6, pp. 2243–2245, 2009, doi: 10.1021/nl900186w.

[21] S. Tottori, L. Zhang, F. Qiu, K. K. Krawczyk, A. Franco-Obregõn, and B. J. Nelson, “Magnetic helical micromachines: Fabrication, controlled swimming, and cargo transport,” *Adv. Mater.*, 2012, doi: 10.1002/adma.201103818.

[22] J. J. Abbott *et al.*, “How Should Microrobots Swim?,” *Int. J. Rob. Res.*, vol. 28, no. 11–12, pp. 1434–1447, Nov. 2009, doi: 10.1177/0278364909341658.

[23] R. Dreyfus, J. Baudry, M. L. Roper, M. Fermigier, H. A. Stone, and J. Bibette, “Microscopic artificial swimmers,” *Nature*, 2005, doi: 10.1038/nature04090.

[24] H. Xu, M. Medina-Sánchez, V. Magdanz, L. Schwarz, F. Hebenstreit, and O. G. Schmidt, “Sperm-Hybrid Micromotor for Targeted Drug Delivery,” *ACS Nano*, vol. 12, no. 1, pp. 327–337, Jan. 2018, doi: 10.1021/acsnano.7b06398.

[25] M. A. Zeeshan *et al.*, “Hybrid helical magnetic microrobots obtained by 3D template-assisted electrodeposition,” *Small*, 2014, doi: 10.1002/smll.201302856.

[26] O. Felfoul *et al.*, “Magneto-aerotactic bacteria deliver drug-containing nanoliposomes to tumour hypoxic regions,” 2016, doi: 10.1038/NNANO.2016.137.

[27] Z. Wu *et al.*, “Turning erythrocytes into functional micromotors,” *ACS Nano*, 2014, doi: 10.1021/nn506200x.

[28] A. Ghosh, P. Mandal, S. Karmakar, and A. Ghosh, “Analytical theory and stability analysis of an elongated nanoscale object under external torque.,” *Phys. Chem. Chem. Phys.*, vol. 15, no. 26, pp. 10817–23, 2013, doi: 10.1039/c3cp50701g.

[29] P. Fischer and A. Ghosh, “Magnetically actuated propulsion at low Reynolds numbers: towards nanoscale control,” *Nanoscale*, vol. 3, no. 2, pp. 557–563, Feb. 2011, doi: 10.1039/C0NR00566E.

[30] A. A. Ghosh, D. Dasgupta, M. Pal, K. I. K. I. Morozov, A. M. A. M. Leshansky, and A. A. Ghosh, “Helical Nanomachines as Mobile Viscometers,” *Adv. Funct. Mater.*, vol. 28, no. 25, p. 1705687, Jun. 2018, doi: 10.1002/adfm.201705687.

[31] M. Pal *et al.*, “Maneuverability of Magnetic Nanomotors Inside Living Cells,” *Adv. Mater.*, vol. 30, no. 22, p. 1800429, May 2018, doi: 10.1002/adma.201800429.

[32] M. Pal *et al.*, “Helical nanobots as mechanical probes of intra- and extracellular environments,” *J. Phys. Condens. Matter*, Jan. 2020, doi: 10.1088/1361-648X/ab6f89.

[33] D. Dasgupta, D. Pally, D. K. Saini, R. Bhat, and A. Ghosh, “Nanomotors Sense Local Physicochemical Heterogeneities in Tumor Microenvironments**,” *Angew. Chemie - Int. Ed.*, 2020, doi: 10.1002/anie.202008681.

[34] P. L. Venugopalan, S. Jain, S. Shivashankar, and A. Ghosh, “Single coating of zinc ferrite renders magnetic nanomotors therapeutic and stable against agglomeration,” *Nanoscale*, vol. 10, no. 5, pp. 2327–2332, Feb. 2018, doi: 10.1039/C7NR08291F.

[35] Z. Wu *et al.*, “A swarm of slippery micropropellers penetrates the vitreous body of the eye,” *Sci. Adv.*, vol. 4, no. 11, p. eaat4388, Nov. 2018, doi: 10.1126/sciadv.aat4388.

[36] D. Walker, B. T. Kasdorf, H.-H. Jeong, O. Lieleg, and P. Fischer, “Enzymatically active biomimetic micropropellers for the penetration of mucin gels,” *Sci. Adv.*, vol. 1, no. 11, p. e1500501, 2015, doi: 10.1126/sciadv.1500501.

[37] S. Ghosh and A. Ghosh, “Mobile nanotweezers for active colloidal manipulation,” *Sci. Robot.*, vol. 3, no. 14, p. eaaq0076, Jan. 2018, doi: 10.1126/scirobotics.aaq0076.

[38] S. Ghosh and A. Ghosh, “All optical dynamic nanomanipulation with active colloidal tweezers,” *Nat. Commun.*, vol. 10, no. 1, p. 4191, Dec. 2019, doi: 10.1038/s41467-019-12217-2.

[39] P. L. Venugopalan, R. Sai, Y. Chandorkar, B. Basu, S. Shivashankar, and A. Ghosh, “Conformal Cytocompatible Ferrite Coatings Facilitate the Realization of a Nanovoyager in Human Blood,” *Nano Lett.*, vol. 14, no. 4, pp. 1968–1975, Apr. 2014, doi: 10.1021/nl404815q.

[40] G. Patil and A. Ghosh, “Anomalous Behavior of Highly Active Helical Swimmers,” *Front. Phys.*, vol. 8, p. 656, Jan. 2021, doi: 10.3389/fphy.2020.628276.

[41] D. Schamel, M. Pfeifer, J. G. Gibbs, B. Miksch, A. G. Mark, and P. Fischer, “Chiral colloidal molecules and observation of the propeller effect,” *J. Am. Chem. Soc.*, 2013, doi: 10.1021/ja405705x.

[42] P. Mandal, V. Chopra, and A. Ghosh, “Independent Positioning of Magnetic Nanomotors,” *ACS Nano*, vol. 9, no. 5, pp. 4717–4725, May 2015, doi: 10.1021/acsnano.5b01518.

[43] P. Mandal and A. Ghosh, “Observation of enhanced diffusivity in magnetically powered reciprocal swimmers,” *Phys. Rev. Lett.*, 2013, doi: 10.1103/PhysRevLett.111.248101.

[44] P. Mandal, G. Patil, H. Kakoty, and A. Ghosh, “Magnetic Active Matter Based on Helical Propulsion,” *Acc. Chem. Res.*, vol. 51, no. 11, pp. 2689–2698, Nov. 2018, doi: 10.1021/acs.accounts.8b00315.

[45] F. J. Vertucci, “Root canal anatomy of the human permanent teeth,” *Oral Surgery, Oral Med. Oral Pathol.*, 1984, doi: 10.1016/0030-4220(84)90085-9.

[46] B. Esteban-Fernández De Ávila *et al.*, “Acoustically Propelled Nanomotors for Intracellular siRNA Delivery,” *ACS Nano*, vol. 10, no. 5, pp. 4997–5005, May 2016, doi: 10.1021/acsnano.6b01415.

[47] L. Baraban *et al.*, “Fuel-free locomotion of janus motors: Magnetically induced thermophoresis,” *ACS Nano*, 2013, doi: 10.1021/nn305726m.

[48] V. Garcia-Gradilla *et al.*, “Functionalized Ultrasound-Propelled Magnetically Guided Nanomotors: Toward Practical Biomedical Applications,” *ACS Nano*, vol. 7, no. 10, pp. 9232–9240, Oct. 2013, doi: 10.1021/nn403851v.

[49] L. Zhang, J. J. Abbott, L. Dong, B. E. Kratochvil, D. Bell, and B. J. Nelson, “Artificial bacterial flagella: Fabrication and magnetic control,” *Appl. Phys. Lett.*, vol. 94, no. 6, p. 064107, Feb. 2009, doi: 10.1063/1.3079655.

[50] P. L. Venugopalan, B. Esteban-Fernández de Ávila, M. Pal, A. Ghosh, and J. Wang, “Fantastic Voyage of Nanomotors into the Cell,” *ACS Nano*, 2020, doi: 10.1021/acsnano.0c05217.

[51] X. Yan *et al.*, “Multifunctional biohybrid magnetite microrobots for imaging-guided therapy,” *Sci. Robot.*, vol. 2, no. 12, p. eaaq1155, Nov. 2017, doi: 10.1126/scirobotics.aaq1155.

[52] F. Ullrich *et al.*, “Mobility Experiments With Microrobots for Minimally Invasive Intraocular

Surgery," *Investig. Opthalmology Vis. Sci.*, vol. 54, no. 4, p. 2853, Apr. 2013, doi: 10.1167/iovs.13-11825.

[53] V. M. Kadiri *et al.*, "Biocompatible Magnetic Micro- and Nanodevices: Fabrication of FePt Nanopropellers and Cell Transfection," *Adv. Mater.*, 2020, doi: 10.1002/adma.202001114.